Journal of Materials Chemistry C

COMMUNICATION

View Article Online
View Journal | View Issue

Cite this: J. Mater. Chem. C, 2015, 3, 1655

Received 9th November 2014
Accepted 14th January 2015

DOI: 10.1039/c4tc02551b

www.rsc.org/MaterialsC

A low-temperature co-precipitation approach to synthesize fluoride phosphors $K_2MF_6:Mn^{4+}$ (M = Ge, Si) for white LED applications†

Ling-Ling Wei,[a] Chun Che Lin,[b] Mu-Huai Fang,[b] Mikhail G. Brik,[cd] Shu-Fen Hu,[e] Huan Jiao*[a] and Ru-Shi Liu*[bf]

A new class of Mn^{4+} activated alkali-metal hexafluoride red phosphors are emerging for white light-emitting diodes because of their sharp red line $^2E_g \rightarrow {}^4A_{2g}$ emissions (600–650 nm) excited by irradiation of $^4A_{2g} \rightarrow {}^4T_{1g}$ (320–380 nm) and $^4A_{2g} \rightarrow {}^4T_{2g}$ (380–500 nm) transitions. However, these phosphors have the drawbacks of difficult control of the Mn valence state during synthesis and lack of underlying mechanisms for structure–photoluminescence relationships. In this study, we explore a novel, highly productive route to the quantifiable synthesis of $K_2GeF_6:Mn^{4+}$ by the chemical co-precipitation method at room temperature. The prepared yellowish $K_2GeF_6:Mn^{4+}$ powders exhibit a hexagonal shape and high crystallinity without significant defects. The photoluminescence thermal stability and white light-emitting diodes applicability of $K_2GeF_6:Mn^{4+}$ suggest that it is a promising commercial red phosphor because of its efficient emission intensity, high color purity and excellent thermal stability. Structural analyses and theoretical calculations reveal that the red shift of the $K_2GeF_6:Mn^{4+}$ red phosphor compared with $K_2SiF_6:Mn^{4+}$ is due to the longer Ge–F distance and lower effective Mulliken charge of F ions in coordination environments of the MnF_6^{2-} octahedron. The split feature in $K_2GeF_6:Mn^{4+}$ is due to the hexagonal distortion in the host. The structure–photoluminescence mechanism is predicted to be general in hexafluoride red phosphors to tune the optical properties through cationic substitutions and crystal structure adjustments.

1. Introduction

To fabricate warm white light-emitting diodes (WLEDs) with a higher color-rendering index (CRI, $R_a > 80$), rare-earth activated nitride red phosphors, such as $MAlSiN_3:Eu^{2+}$ (M = Ca and Sr) and $M_2Si_5N_8:Eu^{2+}$ (M = Ca, Sr, and Ba), are commercially added due to their sufficient chemical durability and efficient luminescent properties.[1–6] But these phosphors suffer from disadvantages as follows: (1) demanding synthesis conditions for isolating from air and moisture increase the production cost; (2) very broad emission spectrum (full width at half maximum ~80 nm) and a large part of the spectrum beyond 650 nm reduces the luminous efficiency of radiation. Hence, alternative red phosphors with high luminescence efficiency from 600 nm to 650 nm, good thermal stability and low production cost should be explored.

Mn^{4+} (electronic configuration, $3d^3$) exhibits sharp emission lines at 600–680 nm because of its distinctive electronic structure. In contrast to the inner 4f → 4f forbidden transition of Eu^{3+}, the outer 3d → 3d transition of Mn^{4+} is sensitive to local crystal field environments in the host and can be tuned by various substitutions.[7–12] Studies have focused on the preparation and optical properties of Mn^{4+} activated fluoride phosphors. Adachi *et al.* synthesized a series of Mn^{4+} activated red fluoride phosphors $A_2XF_6:Mn^{4+}$ (A = K, Na, Cs or NH_4; X = Si, Ge, Zr or Ti) and $BSiF_6:Mn^{4+}$ (B = Ba or Zn) by wet-chemical etching of silicon wafers. However, this method was inappropriate for quantifiable production because of the high cost of metal wafers and low luminescence efficiency caused by difficulty of controlling the valence state of Mn during synthesis.[13–17] The crystal structure of the host and the optical properties of Mn^{4+} emitters in fluoride phosphors remain unclear.[13–19] Hence, the structure–luminescence relationship should be analyzed to properly tune the optical properties of Mn^{4+} activated fluoride phosphors and meet the requirements of red phosphor. The characteristics and drawbacks of $K_2GeF_6:Mn^{4+}$ and other red phosphors are compared differently in Table S1.† It points on how $K_2GeF_6:Mn^{4+}$ overcomes the drawbacks that other red phosphors have.

[a]School of Chemistry and Chemical Engineering, Shaanxi Normal University, Xi'an 710062, Shaanxi, P. R. China. E-mail: jiaohuan@snnu.edu.cn

[b]Department of Chemistry, National Taiwan University, Taipei 106, Taiwan. E-mail: rsliu@ntu.edu.tw

[c]College of Sciences, Chongqing University of Posts and Telecommunications, Chongqing 400065, P. R. China

[d]Institute of Physics, University of Tartu, Ravila 14C, Tartu, 50411, Estonia

[e]Department of Physics, National Taiwan Normal University, Taipei 116, Taiwan

[f]Department of Mechanical Engineering and Graduate Institute of Manufacturing Technology, National Taipei University of Technology, Taipei 106, Taiwan

† Electronic supplementary information (ESI) available. See DOI: 10.1039/c4tc02551b

In this study, we used the chemical co-precipitation method to synthesize $K_2GeF_6:Mn^{4+}$ with high purity and good crystallinity without significant defects. The prepared yellowish $K_2GeF_6:Mn^{4+}$ powders exhibited an efficient emission intensity, high color purity and excellent thermal stability; these substances could be used in commercial applications. As the germanium oxide is easily dissolved in concentrated HF solution, the novel chemical co-precipitation method was operated at room temperature and suitable for quantifiable production because of its high yield, good repeatability and low cost. Particularly, in order to analyze the effects of the host crystal structure on the optical properties of Mn^{4+} emitters, the crystal field and *ab inito* calculations combined with synchrotron X-ray diffraction (XRD) refinement and extended X-ray absorption fine structure (EXAFS) analysis were used to probe the optical features of $K_2GeF_6:Mn^{4+}$ and $K_2SiF_6:Mn^{4+}$.

The valence states of Mn (2^+, 3^+, 4^+, 6^+ and 7^+) are sensitive to the synthesis temperature. Hence, the main difficulty lies in controlling the Mn valence state for synthesizing Mn^{4+} activated fluoride compounds.[19] Thus a two-step strategy of synthesizing K_2MnF_6 initially and then precipitating $K_2(Ge/Si)F_6:Mn^{4+}$ was proposed, and the synthesis temperature was not higher than 55 °C to avoid Mn^{4+} reduction. The specific operation route is shown in the ESI.† Fig. S1–S3† reveal that the synthesis temperature can tune the emission intensity of $K_2(Ge/Si)F_6:Mn^{4+}$ red phosphors by synchronously controlling the morphology and valence state of Mn. The optimal synthesis temperature for $K_2GeF_6:Mn^{4+}$ and $K_2SiF_6:Mn^{4+}$ red phosphors are 25 °C and 52 °C, respectively; these phosphors were used to investigate the structural and optical properties in this study. The two-step chemical co-precipitation strategy to synthesize $K_2GeF_6:Mn^{4+}$ red phosphor exhibits the following advantages: (1) the optimal synthesis temperature is room temperature, which can effectively reduce the volatilization of HF; (2) the amount of HF consumed to synthesize $K_2GeF_6:Mn^{4+}$ red phosphor is half of that used to synthesize $K_2SiF_6:Mn^{4+}$, which is safe and environmentally friendly; (3) $K_2GeF_6:Mn^{4+}$ red phosphor synthesized by a two-step chemical co-precipitation method at room temperature exhibits efficient emission intensity and high thermal stability, which are beneficial to commercial applications.

2. Experimental

A two-step chemical co-precipitation method was used to synthesize $K_2(Ge/Si)F_6:Mn^{4+}$ red phosphors by initially synthesizing K_2MnF_6 and then precipitating $K_2(Ge/Si)F_6:Mn^{4+}$.

(1) Synthesis of K_2MnF_6

High-purity $KMnO_4$ and KHF_2 with a mass ratio of 1 : 20 were dissolved in aqueous HF (48%) solution. The mixed solution was stirred and cooled for 0.5 h. The yellow powder K_2MnF_6 was precipitated by slowly adding H_2O_2. After fast filtering and washing by acetone, the yellow powder was oven-dried for 2 h.

(2) Synthesis of $K_2(Ge/Si)_{0.95}F_6:Mn_{0.05}{}^{4+}$

GeO_2 (2.78 g) and KF (4.65 g) were dissolved in 15 mL HF (48%) aqueous solution at room temperature. After adding 0.2 g of K_2MnF_6 powders in GeO_2–HF aqueous solution, the mixed solution was stirred at room temperature or in a water bath with a fixed temperature between 0 °C and 60 °C. The KF–HF solution was added dropwise to the brown GeO_2–HF–K_2MnF_6 solution to precipitate a yellow powder at the bottom of the container. Accordingly, the color of the mixture solution changed from brown to almost colorless. After pouring out the supernatant and washing thrice with ethanol, the yellow precipitate was oven-dried for 2 h. However, for the synthesis of $K_2Si_{0.95}F_6:Mn_{0.05}{}^{4+}$, 1.60 g SiO_2 was dissolved in 35 mL HF (48%) aqueous solution in a bath water at 70 °C. Other procedures were similar to the synthesis of $K_2Ge_{0.95}F_6:Mn_{0.05}{}^{4+}$.

(3) Structural and optical characterization

Synchrotron X-ray diffraction (XRD) patterns of the samples were collected with a Debye–Scherrer camera installed at the BL01C2 beamline of the National Synchrotron Radiation Research Center (NSRRC, Taiwan) with 0.774907 Å wavelength. General Structure Analysis System software was used to analyse the X-ray Rietveld profile refinements of the structural modes. The extended X-ray absorption fine structure spectroscopy (EXAFS) results of Ge K-edge and Si K-edge were obtained at the BL01C and BL16A beamline stations of NSRRC, respectively. The morphologies of the samples were characterized using a scanning electron microscope (SEM, JSM-6700F). High-resolution transmission electron microscopy and selected area electron diffraction images were obtained using a JEOL JEM-2011 microscope operating at 200 kV. The RT excitation and emission spectra were measured using a FluoroMax-3 spectrophotometer equipped with a 150 W Xe lamp. For temperature-dependent experiments at 80–300 K, the samples were placed in a small hold, the temperature of which was controlled by a liquid nitrogen cooling device. Light was radiated using a Hamamatsu R928 photo-multiplier tube. The THMS-600 heating device was also used to study thermal quenching above 300 K.

3. Results and discussion

Fig. 1(a) and (b) respectively show the X-ray Rietveld refinement results and the crystal structure of $K_2GeF_6:Mn^{4+}$. Fig. S4† illustrates the related structural results of $K_2SiF_6:Mn^{4+}$. Yellowish $K_2GeF_6:Mn^{4+}$ powders yield bright red emission upon excitation of 460 nm light, indicating that Mn^{4+} successfully doped into the crystal lattice of K_2GeF_6. The diffraction peaks of $K_2GeF_6:Mn^{4+}$ phosphor can be indexed to the hexagonal $P\bar{3}m1$ space group with lattice parameters of $a = b = 5.63171$ (6) Å, $c = 4.66751$ (6) Å, $\alpha = \beta = 90°$, $\gamma = 120°$ and $V = 128.2027$ (20) Å^3 (JCPDS no. 73-1531). No traces of residual K_2MnF_6 and other impurities are observed. The crystal structure (Fig. 1(b)) shows that each Ge^{4+} is surrounded by 6 F^- to form a regular $GeF_6{}^{2-}$ octahedron. K^+ is at the center of 12 neighbouring F^-. The prepared $K_2SiF_6:Mn^{4+}$ powders show a lighter color than $K_2GeF_6:Mn^{4+}$, and emit bright red light under excitation of

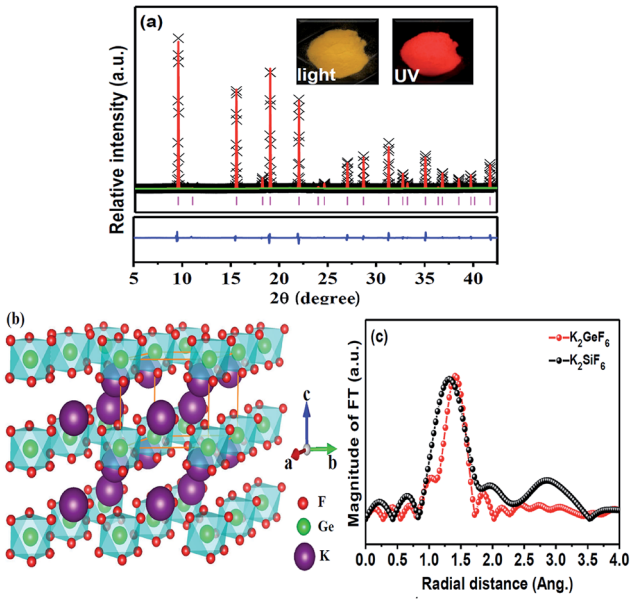

Fig. 1 Structural results of K_2GeF_6:Mn^{4+} phosphor. (a) X-Ray Rietveld refinements of K_2GeF_6:Mn^{4+}. (b) Structural schematic diagrams. (c) Fourier-transform-fitted EXAFS spectra for K_2GeF_6:Mn^{4+} and K_2SiF_6:Mn^{4+}.

460 nm light. The K_2SiF_6:Mn^{4+} phosphor exhibits a high purity and belongs to the cubic *Fm3m* space group with lattice parameters of $a = b = c = 8.13107\ (7)$ Å, $\alpha = \beta = \gamma = 90°$ and $V = 537.579\ (8)$ Å^3 (JCPDS no. 37-1155; Fig. S4†). Si^{4+} resides in the vertex and face-centered position of the cubic unit cell; and 4 K^+ ions are uniformly distributed inside the cube. Each Si^{4+} is surrounded by 6 F^- to form a regular SiF_6^{2-} octahedron. Furthermore, central Ge^{4+} and Si^{4+} possess different coordination environments as GeF_6^{2-} and SiF_6^{2-} octahedrons lie in various crystal structures. Measurements of the extended X-ray absorption fine structure (EXAFS) associated with Fourier-transform fitting were used to analyze the coordination environments of Ge^{4+} and Si^{4+}. Fig. 1(c) suggests that the bond length between Ge^{4+} and ligand F^- ions (1.81 Å) is longer than that between Si^{4+} and F^- ions (1.66 Å). The differences between K_2GeF_6:Mn^{4+} and K_2SiF_6:Mn^{4+} phosphors in a coordination environment and lattice symmetry of the host structure significantly influence their optical properties.

The microstructures of K_2GeF_6:Mn^{4+} were examined using scanning electron microscopy (SEM) and high resolution transmission electron microscopy (HRTEM). SEM images indicate that the K_2GeF_6:Mn^{4+} powders show a hexagonal shape, and their sizes range from 20 μm to 50 μm. By contrast, K_2SiF_6:Mn^{4+} powders (Fig. S4(c)†) are octahedral in shape and the particle sizes are in the range of 10–30 μm. Typical HRTEM images reveal a very fine lattice arrangement of K_2GeF_6:Mn^{4+}, indicating a single crystal structure with high crystallinity and low structural defects. The selected area electron diffraction image (SAED; inset Fig. 2(b)) exhibits specific shell-shaped-pattern spots corresponding to the [111] zone axis of the hexagonal $P\bar{3}m1$ space group. The crystal lattice spacing of the $(\bar{2}20)$ plane is about 0.24 nm, which is consistent with the XRD

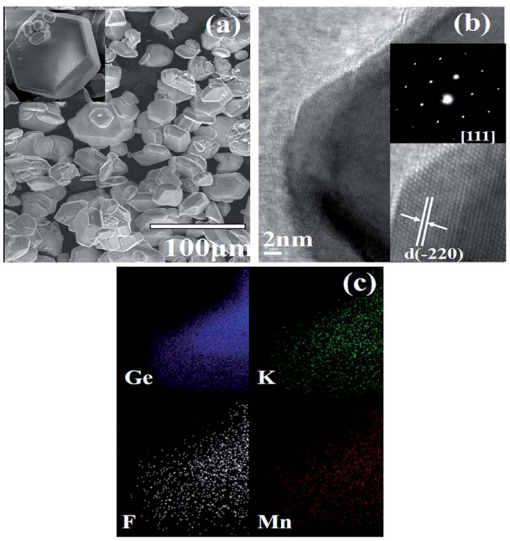

Fig. 2 (a) SEM images and (b) HRTEM images of K_2GeF_6:Mn^{4+} phosphor; (inset) SAED pattern along the [111] zone axis. (c) Element mapping images of Ge, K, F, and Mn for K_2GeF_6:Mn^{4+}.

results. Fig. 2(c) shows the element mapping images of Ge, K, F and Mn for K_2GeF_6:Mn^{4+}. All elements show uniform distributions in the image contours, and the shapes of mapping images match well with the HRTEM images.

Fig. 3(a) illustrates the excitation and emission spectra of K_2GeF_6:Mn^{4+} and K_2SiF_6:Mn^{4+} red phosphors measured at room temperature. Consistent with the reported results of other Mn^{4+} activated fluoride compounds, there are two broad excitation bands located in the range of 320–500 nm, corresponding to the spin-allowed transitions of $^4A_{2g} \rightarrow {}^4T_{1g}$ and $^4A_{2g} \rightarrow {}^4T_{2g}$, respectively. The sharp red emission lines in the range of 600–650 nm originated from the spin-forbidden $^2E_g \rightarrow {}^4A_{2g}$ transition. Different from the $^4A_{2g} \rightarrow {}^4T_{1g}$ transition spectra, the $^4A_{2g} \rightarrow {}^4T_{2g}$ transition of K_2GeF_6:Mn^{4+} and K_2SiF_6:Mn^{4+} red phosphors show several occasional sharp peaks that are attributed to the asymmetric vibronic progression of the MnF_6 octahedron supposed on the electronic transition.[14] More importantly, the excitation and emission spectra of K_2GeF_6:Mn^{4+} exhibit a red shift compared to K_2SiF_6:Mn^{4+}.

To analyze the red shift behaviour of K_2GeF_6:Mn^{4+}, crystal field calculations of the Mn^{4+} energy levels in K_2GeF_6 and K_2SiF_6 were obtained by diagonalizing the following crystal field Hamiltonian (ESI†).[20] The calculated energy levels (Table 1) reconfirm the red shift of K_2GeF_6:Mn^{4+} phosphor. All the orbital triplets in K_2GeF_6 are split into singlets and doublets, as it should be in a hexagonal crystal field. While all orbital triplets are not split in cubic K_2SiF_6 since the octahedral symmetry is preserved at the Si position. The first explanation for the red shift is that the electronic density in K_2GeF_6 is higher than it is in K_2SiF_6. It results in red-shifted energy levels and excitation peaks as shown in Table 1. *Ab initio* calculations have been indispensably used to assess the perspectives of material applications and limitations. We also used the CASTEP module of Materials Studio package.[21] Diagrams of the partial density of states (DOS; Fig. 3(b)) allow the identification of the lowest

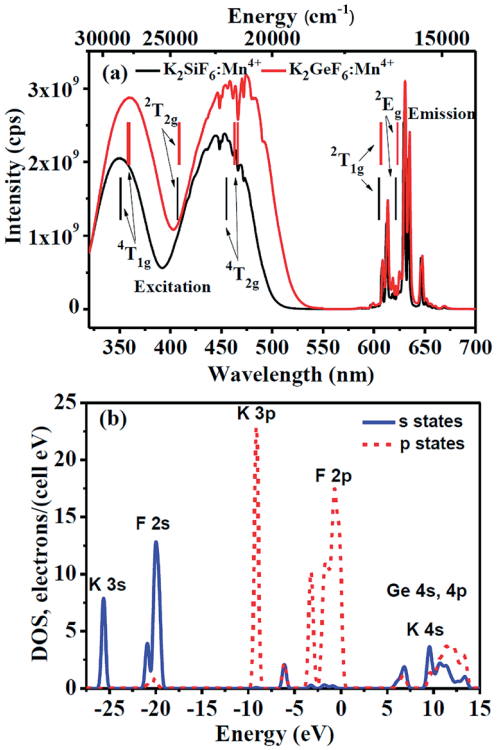

Fig. 3 (a) Experimental excitation and emission spectra of K_2GeF_6:Mn^{4+} and K_2SiF_6:Mn^{4+} phosphors (solid lines) compared with the calculated energy levels of Mn^{4+} (vertical bars). (b) Calculated partial DOS diagrams for K_2GeF_6.

Table 1 Calculated and experimental energy levels (in cm^{-1}) for Mn^{4+} in K_2GeF_6 and K_2SiF_6. The orbital doublet states are denoted with an asterisk. The Racah parameters are also given

	K_2GeF_6 (B = 590; C = 3831)		K_2SiF_6 (B = 605; C = 3806)	
O_h group "parent" LS term	Calc.	Exp.	Calc.	Exp.
$^4A_{2g}$ (^4F)	0	0	0	0
^2E_g (^2G)	16 050*	16 050	16 091	16 091
$^2T_{1g}$ (^2G)	16 477*, 16 489		16 534	
$^4T_{2g}$ (^4F)	21 454*, 21 598	~21 505	21 977	~21 978
$^2T_{2g}$ (^2G)	24 462, 24 488*		24 573	
$^4T_{1g}$ (^4F)	27 808, 27 922*	~27 866	28 475	~28 490
$^4T_{1g}$ (^4P)	45 415*, 45 723		46 530	

electronic states in the K_2GeF_6 conduction band as those arising from the mixture of the K and Ge 4s states. The F 2p states, which are dominant in the valence band of both crystals, make a minor contribution to the conduction band due to the hybridization effects. Very sharp (strongly localized) 3s and 3p electronic states of K and 2s states of F form narrow electronic bands at high energies. The effective Mulliken charges for all ions were calculated from the generalized gradient approximation (GGA) and local density approximation (LDA; Table S6†). The absolute value of the effective fluorine charge in K_2GeF_6 is smaller than that in K_2SiF_6, which contributes to the weak crystal field in the former host and strong one in the latter host. Therefore, the red shifts of all K_2GeF_6:Mn^{4+} spectral bands are consistently explained from the results of *ab initio* calculations.

Except for the red shift, another interesting phenomenon is also found for K_2GeF_6:Mn^{4+} red phosphor: broader excitation and emission bands compared with K_2SiF_6:Mn^{4+}. The peak positions are dependent on the coordination environments of the MnF_6^{2-} octahedron, while the shape of emission spectra is associated with the crystal structure of the host. Mn^{4+} ions in the K_2SiF_6 host with the $Fm3m$ space group have O_h symmetry, whereas the site symmetry of Mn^{4+} ions in the K_2GeF_6 host with the $P\bar{3}m1$ space group reduces to D_{3d}. The octahedral symmetry of O_h exhibits 6 fundamental internal vibronic modes ν_1 (A_{1g}), ν_2 (E_g), ν_3 (T_{1u}), ν_4 (T_{1u}), ν_5 (T_{2g}) and ν_6 (T_{2u}). The ungerade vibrations of ν_3, ν_4 and ν_6 introduce some u characters into the ^2E_g wave functions and then produce the dipole allowed transition. In D_{3d} symmetry, the triply degenerate modes of ν_3, ν_4, ν_5 and ν_6 will split into doubly degenerate and non-degenerate modes as a result of small hexagonal distortion,[19] which results in stronger vibration transition coupling and broad emission lines.

To further reveal the electronic and vibronic structures of Mn^{4+} ions in different hosts, the temperature-dependent photoluminescence (PL) spectra were measured and are shown in Fig. S6.† The integrated area of emission increases gradually between 80 K and 300 K in both K_2GeF_6:Mn^{4+} and K_2SiF_6:Mn^{4+} systems. The decreasing curve of K_2GeF_6:Mn^{4+} is observed at temperatures over 300 K. However, it is interesting that the decreasing curve of K_2SiF_6:Mn^{4+} is demonstrated at higher temperatures over 470 K. Both of them have high thermal stability at an LED operation temperature (150 °C), and the intensity of emission is still over 90% of them at room temperature. Fig. 4(a) and S7† respectively show the wavelength position and relative intensity of each emission line obtained at different temperatures for K_2GeF_6:Mn^{4+} and K_2SiF_6:Mn^{4+} red phosphors. The common feature is that all emission peaks show slight red shift and become broader with increasing temperature, which is reasonable as that the unit cell expands and the vibration modes enhance under heat treatment. K_2GeF_6:Mn^{4+} exhibit unique split feature of peaks located at 610.0 nm, 610.3 nm, 635.0 nm and 647.0 nm, corresponding to the anti-Stokes ν_4, ν_6 and Stokes ν_4, ν_3 local vibronic emission peaks. The fundamental lattice modes of the transverse acoustic (TA) are more noticeable for Mn^{4+} in the hexagonal K_2GeF_6 host with low crystal symmetry. The temperature-dependent behavior of integrated PL intensity I_{PL} (Fig. 4(b)) shows a considerable amount of stability for K_2GeF_6:Mn^{4+} red phosphor in the temperature range of 120–420 K. The relative I_{PL} at 420 K is above 96%, which is higher than that of rare-earth doped inorganic phosphors. As the vibronic emissions dominate the PL spectra of Mn^{4+} in fluorides, both the emission intensity and emission shape are responsible for the I_{PL} intensity. With increasing temperature from 80 K to 270 K, the anti-Stokes emissions increase dramatically and all emission lines become broader as a result of the increased absorbed photons and enhanced vibration transition coupling associated with the vibration modes of MnF_6^{2-} octahedron, leading to the slight

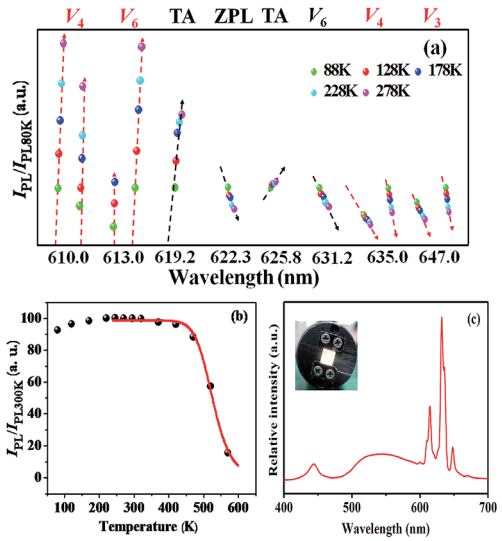

Fig. 4 (a) The wavelength position and relative intensity of each emission line obtained at different temperatures for K_2GeF_6:Mn^{4+} red phosphor. (b) Temperature dependence of integrated PL intensity relative to room temperature for K_2GeF_6:Mn^{4+}. (c) Luminescence spectra of the white LEDs used K_2GeF_6:Mn^{4+} red phosphor (inset: WLED image).

increase of I_{PL} intensity. A further increase in the temperature above 300 K will increase the non-radiative transition probability and the I_{PL} intensity shows thermal quenching, which can be fitted by $I_T/I_0 = [1 + D\exp(-E_a/kT)]^{-1}$, where I_0 is the intensity at $T = 0$ K, D and activation energy E_a are refined variables. The activation energies obtained for K_2GeF_6:Mn^{4+} red phosphor is 0.93 eV, which is 4 times higher than that of nitride compounds (~0.23 eV). Moreover, the external quantum efficiency of K_2GeF_6:Mn^{4+} is 54% at room temperature. To evaluate the commercial application of the synthesized K_2GeF_6:Mn^{4+} phosphor, the performances of WLEDs (fabricated with blue InGaN chips, $Y_3Al_5O_{12}$:Ce^{3+} yellow phosphor and K_2GeF_6:Mn^{4+} red phosphor) were examined. Electroluminescence spectra of the WLEDs reconfirm the sharp emission lines of Mn^{4+} in K_2GeF_6 phosphor. A bright "warm" white light with a CRI of 89 is obtained under a drive current of 15 mA (Fig. 4(c)). The chromaticity coordinates of (0.4016, 0.4495) lie near the black body locus and the color temperature for WLEDs is 3974 K. Both the thermal stability and package results indicate the great potential of K_2GeF_6:Mn^{4+} as commercial red phosphor in warm WLEDs.

4. Conclusions

In summary, the chemical co-precipitation method was used to synthesize the K_2GeF_6:Mn^{4+} red phosphor with high purity and good crystallinity without significant defects. This method operated at room temperature was suitable for quantifiable production due to its high yield, good repeatability and low cost. The prepared yellowish K_2GeF_6:Mn^{4+} powders had great potential as a commercial red phosphor thanks to their efficient emission intensity, high color purity and excellent thermal stability. The structural analysis and theoretical calculations showed that the optical properties of Mn^{4+} activated fluoride phosphors were associated with the coordination environments of the MnF_6^{2-} octahedron. The split feature in K_2GeF_6:Mn^{4+} was caused by hexagonal distortion in the host. The structure–photoluminescence mechanism was predicted to be general in hexafluoride red phosphors to tune the optical properties through cation substitutions and crystal structure adjustments.

Acknowledgements

The authors would like to thank the National Science Council of the Ministry of Science and Technology of Taiwan (Contracts nos MOST 103-2112-M-003-009-MY3 and MOST 101-2113-M-002-014-MY3) for financially supporting this work. The financial support from the Industrial Technology Research Institute of Taiwan under the contract number of D351A41300 is also appreciated. M. G. Brik appreciates support from the Marie Curie Initial Training Network LUMINET (grant agreement no. 316906), and the Programme for the Foreign Experts offered by Chongqing University of Posts and Telecommunications. We also thank Dr G. A. Kumar (University of Texas at San Antonio) for allowing us to use the Materials Studio package. Huan Jiao is grateful for financial support by the National Natural Science Foundation of China (nos 51272151) and the Fundamental Research Fund for the Central Universities (nos GK201402052, and GK201305013). Support by the CAS/SAFEA International Partnership Program for Creative Research Teams is also appreciated.

References

1 J. Li, T. Watanabe, N. Sakamoto, H. Wada, T. Setoyama and M. Yoshimura, *Chem. Mater.*, 2008, **20**, 2095–2105.
2 Y. Q. Li, N. Hirosaki, R. J. Xie, T. Takeda and M. Mitomo, *J. Solid State Chem.*, 2009, **182**, 301–311.
3 M. Zeuner, P. J. Schmidt and W. Schnick, *Chem. Mater.*, 2009, **21**, 2467–2473.
4 Z. J. Zhang, O. M. Ten Kate, A. C. A. Delsing, M. J. H. Stevens, J. T. Zhao, P. H. L. Notten, P. Dorenbos and H. T. Hintzen, *J. Mater. Chem.*, 2012, **22**, 23871–23876.
5 N. Tapia-Ruiz, M. Segales and D. H. Gregory, *Coord. Chem. Rev.*, 2013, **257**, 1978–2014.
6 S. S. Wang, W. T. Chen, Y. Li, J. Wang, H. S. Sheu and R. S. Liu, *J. Am. Chem. Soc.*, 2013, **135**, 12504–12507.
7 Z. Bryknar, V. Trepakov, Z. Potucek and L. Jastrabik, *J. Lumin.*, 2000, **87**, 605–607.
8 Y. Zhydachevskii, D. Galanciak, S. Kobyakov, M. Berkowski, A. Kaminska, A. Suchocki, Y. Zakharko and A. Durygin, *J. Phys.: Condens. Matter*, 2006, **18**, 11385–11396.
9 A. A. Setlur, E. V. Radkov, C. S. Henderson, J. H. Her, A. M. Srivastava, N. Karkada, M. S. Kishore, N. P. Kumar, D. Aesram, A. Deshpande, B. Kolodin, L. S. Grigorov and U. Happek, *Chem. Mater.*, 2010, **22**, 4076–4082.
10 Y. Arai and S. Adachi, *J. Lumin.*, 2011, **131**, 2652–2660.
11 M. G. Brik and A. M. Srivastava, *Opt. Mater.*, 2013, **35**, 1251–1256.
12 M. H. Du, *J. Mater. Chem. C*, 2014, **2**, 2475–2481.

13 T. Takahashi and S. Adachi, *J. Electrochem. Soc.*, 2008, **155**, E183–E188.
14 S. Adachi and T. Takahashi, *J. Appl. Phys.*, 2009, **106**, 013516.
15 Y. K. Xu and S. Adachi, *J. Electrochem. Soc.*, 2011, **158**, J58–J65.
16 R. Kasa and S. Adachi, *J. Electrochem. Soc.*, 2012, **159**, J89–J95.
17 D. Sekiguchi, J. I. Nara and S. Adachi, *J. Appl. Phys.*, 2013, **113**, 183516.
18 L. F. Lv, X. Y. Jiang, S. M. Huang, X. A. Chen and Y. X. Pan, *J. Mater. Chem. C*, 2014, **2**, 3879–3884.
19 H. M. Zhu, C. C. Lin, W. Q. Luo, S. T. Shu, Z. G. Liu, M. Wang, J. T. Kong, E. Ma, Y. G. Cao, R. S. Liu and X. Y. Chen, *Nat. Commun.*, 2014, **5**, 4312.
20 B. Z. Malkin, A. A. Kaplyanskii and B. M. Macfarlane, *Spectroscopy of Solids Containing Rare-earth Ions*, North-Holland, Amsterdam, 1987; p. 13.
21 S. J. Clark, M. D. Segall, C. J. Pickard, P. J. Hasnip, M. J. Probert, K. Refson and M. C. Payne, *Z. Kristallogr. NCS.*, 2005, **220**, 567–568.